Collisions between ^{48}Ti + ^{93}Nb at 917 MeV

T. Kozik
Institute of Physics, Jagellonian University, ul. Reymonta 4, 30-059 Kraków, Poland

V. Abenante, R. J. Charity, A. Chbihi,* Z. Majka,† N. G. Nicolis,‡ D. G. Sarantites, L. G. Sobotka, and D. W. Stracener§
Department of Chemistry, Washington University, St. Louis, Missouri 63130

C. Baktash, M. L. Halbert, and D. C. Hensley
Oak Ridge National Laboratory, Oak Ridge, Tennessee 37831

J. Łukasik
H. Niewodniczanski Institute of Nuclear Physics, ul. Radzikowskiego 152, 31-342 Kraków, Poland
(Received 6 November 1995)

Collisions between ^{48}Ti + ^{93}Nb at 19.1 MeV/nucleon were studied using two 4π detection systems. A reconstruction procedure was developed to determine the mass, kinetic, and excitation energies of the primary projectile and targetlike fragments. The results show a broad range of mechanisms. These results were compared with predictions of the quantum-molecular dynamics model. [S0556-2813(96)05212-0]

PACS number(s): 25.70.Gh, 25.70.Jj, 02.70.Ns, 24.60.Dr

I. INTRODUCTION

One of the most striking findings in the early days of low-energy, heavy-ion nuclear physics was the observation of deep inelastic collisions (DIC) [1]. These reactions can make up a substantial fraction of the total reaction cross section and are characterized by the conversion of a large amount of the relative kinetic energy into internal excitations of the colliding nuclei without obliterating the identity of the projectile and target. With increasing bombarding energy, the reaction picture becomes considerably more complex. New phenomena, such as preequilibrium emission [2], intermediate mass fragment (IMF) emission [3], and projectile breakup [4] enter the reaction process. However, the recent experiment on intermediate-energy, heavy-ion reactions by Lott *et al.* [5] indicates that the collisions of ^{136}Xe + ^{209}Bi at 28.2 MeV/nucleon are predominantly of a binary nature leading to highly excited massive primary projectilelike (PLF) and targetlike fragments (TLF). Surprisingly, this binary character persists for collisions at 45 MeV/nucleon [6] even when a large number of the IMF's are observed. The binary dissipative processes were observed recently at energies approaching 100 MeV/nucleon [7] and at 29 MeV/nucleon in collisions of very heavy nuclei [8]. The important characteristics of these strongly damped reactions are the partition of the mass, charge, excitation energy, and angular momentum between the PLF's and TLF's. Despite the obvious importance of the DIC process, a complete understanding of it is far from being achieved.

In this article, we report on the excitation energy partition in the ^{48}Ti + ^{93}Nb reaction at 19.1 MeV/nucleon. Experimental studies of the excitation energy acquired by the primary PLF's and TLF's, as a function of the total kinetic energy loss, are important because they provide information on the mechanism for the conversion of kinetic energy into internal excitation [9–11]. However, the experimental information about the primary fragments is obscured by their subsequent decay. Thus, in order to reconcile the measured postevaporative fragments with the primary reaction products, complicated reconstruction procedures must be invented. This is done in the present work and the experimental results are compared to dynamical calculations which utilizes a quantum-molecular dynamics concept.

The paper is organized as follows. In Sec. II we sketch the experimental procedures and the detection systems. The experimental results which include selected PLF energy spectra, the light charged particle (LCP) and neutron multiplicities, and γ-ray fold distributions are presented in Sec. III. An event reconstruction procedure is described in the first part of Sec. IV. In the second part of Sec. IV, the primary fragment characteristics are given. The reconstructed experimental data are compared to the molecular dynamics model calculations in Sec. V. Finally, the conclusions are summarized in Sec. VI.

II. EXPERIMENTAL PROCEDURE

The experimental setup consisted of two 4π detection systems. A small highly segmented CsI(Tl) system called the ''Dwarf Ball-Wall'' (DBW) [12] was used to detect the light charged particles (LCP) and intermediate mass fragments ($3 \leqslant Z_{IMF} \leqslant 25$). The most forward part of this device, called the ''Dwarf Wall'' (DW), consists of 40 detectors and covers 4–36 deg in the laboratory frame. The ''Dwarf Ball'' (DB) consists of 62 detectors. The DBW system was placed inside

*Present address: GANIL, Caen, France.

†On leave from Institute of Physics, Jagellonian University, Kraków, Poland.

‡Present address: Department of Physics, University of Ioannina, Greece.

§Present address: Oak Ridge National Laboratory, Oak Ridge, TN 37831.

the Oak Ridge Spin Spectrometer (SS) array [13], a 72-element 4π detection system, which measured the total γ-ray energy and multiplicity as well as the neutron angular distributions and multiplicities. Both systems were triggered by the detection of IMF's in the DW. The events with two IMF detected have been studied in a separate paper [14].

The 917-MeV (19.1 MeV/nucleon) ^{48}Ti beam was provided by the Holifield Heavy-Ion Research Facility using the tandem heavy-ion accelerator coupled to the Oak Ridge Isochronous Cyclotron (ORIC). A self-supporting ^{93}Nb target was used with thickness of 991 μg/cm^2. The beam spot diameter was $\sim$ 2 mm and permitted us to bombard the target at five consecutively different positions, which allowed us to minimize carbon deposits on the ^{93}Nb foil.

The LCP identification was accomplished by pulse-shape discrimination of the CsI(Tl) light output and IMF identification was obtained from both the fast plastic and CsI(Tl) light output. The hydrogen isotopes detected in the DB were energy calibrated using 14 and 24 MeV proton beams elastically and inelastically scattered off a ^{12}C target. The energy calibration of the DW also utilized the observed and calculated punch through pulse heights and energies for hydrogen isotopes. The energy calibration then was extended to the IMF's [12]. All elements were separated as well as hydrogen isotopes in the DB. However, we were not able to separate the hydrogen isotopes in the DW detectors.

The NaI(Tl) detectors of the SS were energy calibrated using radioactive sources. Neutron and γ-ray pulses were distinguished by the time-of-flight method. Since the CsI(Tl) detection system employed leading-edge discriminators and light ions deposited little energy in the fast plastic, additional time walk corrections had to be made in order to achieve neutron-γ separation.

III. EXPERIMENTAL RESULTS

The events recorded had at least one IMF detected in the DW. The detectors of the DW were arranged into five rings positioned at the polar angles 8.4°, 14.8°, 22.4°, 23.2°, and 31.0°. We found that about 12% and 3% of all recorded events had, respectively, two or more IMF's detected in the DW. The experimental results and analysis reported here include events where only one of the IMF's was detected in the DW. This IMF will be called the projectilelike fragment (PLF).

Figure 1 shows the element distributions of the PLF's recorded at 8.4° and 14.8°. In order to make the analysis tractable, only two PLF triggers were selected, namely, $Z_{\mathrm{PLF}} = 11$, which contains only half of the projectile charge and $Z_{\mathrm{PLF}} = 20$, which is close to the projectile charge. The angular distributions of these two PLF's are displayed in Fig. 2 and the energy spectra detected in the second ring of the DW (14.8°) are shown in Fig. 3. The arrows in Fig. 3 indicate the energy corresponding to the beam velocity assuming $A_{\mathrm{PLF}}=2Z_{\mathrm{PLF}}+1$. The PLF energy spectra were divided into four and five bins for $Z_{\mathrm{PLF}} = 11$ and $Z_{\mathrm{PLF}} = 20$, respectively. These bins are separated by the vertical dashed lines in Fig. 3. Analyses were performed by sorting the events according to the detection angle, charge, and energy bin of the PLF trigger.

In order to recognize the emission pattern of the LCP's,

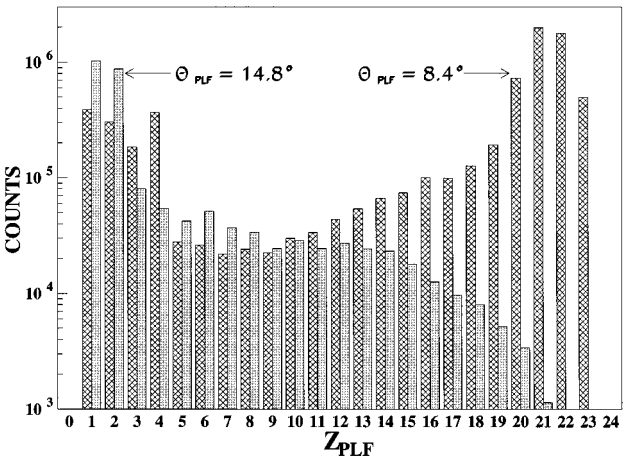

FIG. 1. Element distributions of the PLF's recorded at 8.4° and 14.8°.

Fig. 4 shows polar plots of the invariant cross section as a function of longitudinal (V_L) and transversal (V_T) components of velocity for (a) protons and (b) α-particles detected in coincidence with $Z_{\mathrm{PLF}} = 20$ observed at 14.8° for the lowest-energy bin. The LCP detectors that were within $\pm 30°$ of the reaction plane were selected. Note the isotropic emission from the TLF in the backward hemisphere ($\theta > 60°$) and a more complex picture in the forward hemisphere. The proton and α-particle multiplicities recorded by the DBW in coincidence with $Z_{\mathrm{PLF}} = 11$ and 20 as a function of the PLF energy are displayed (solid circles) in Figs. 5 and 6, respectively. The multiplicities recorded for polar angle $\theta > 60°$ (squares) were used to deduce the total LCP multiplicities associated with the emission from the TLF (tri-

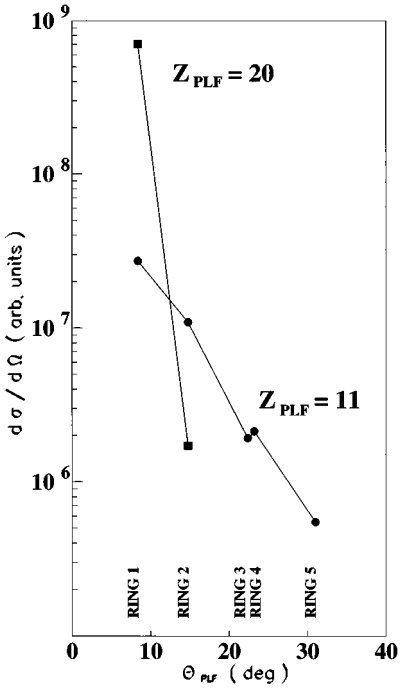

FIG. 2. Angular distributions of the $Z_{\mathrm{PLF}} = 11$ (circles) and 20 (squares) fragments in the laboratory frame. The lines connecting the points is to guide the eye.

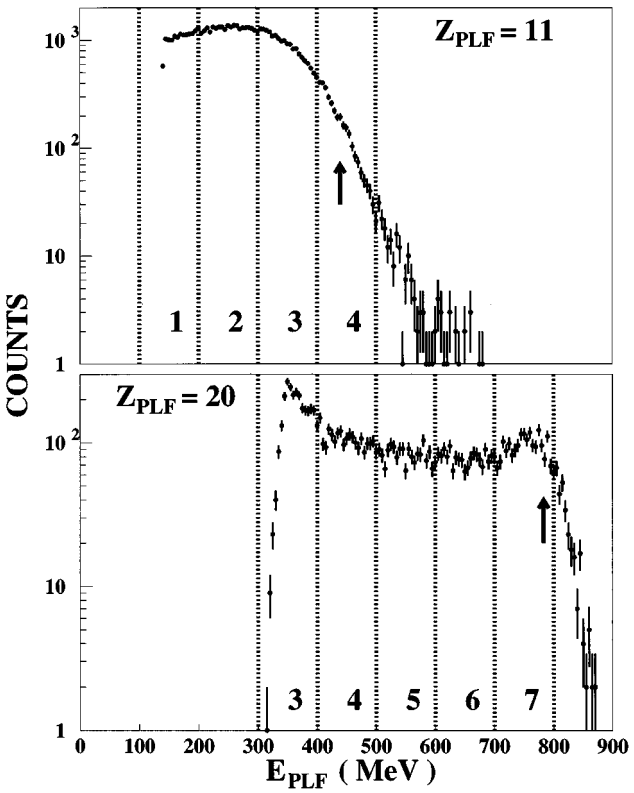

FIG. 3. Energy spectra of the $Z_{PLF} = 11$ and 20 fragments detected in the second ring of the DW detectors. The arrows indicate the energy corresponding to the beam velocity assuming $A_{PLF} = 2Z_{PLF} + 1$. The energy bins used in the analysis are indicated by the vertical dashed lines as numbered.

angles). Here we note that the proton and α-particle emission from the TLF increases with decreasing PLF energy (more damped collisions).

The normalized neutron fold distributions measured in coincidence with the PLF's having kinetic energies from the lowest- and highest-energy bins, respectively, are displayed in Fig. 7. The neutron data were used to obtain the average neutron multiplicities associated with the TLF emission using the procedure discussed in Ref. [10]. Derived neutron multiplicities associated with emission from the TLF, as a function of the PLF energy, are presented as triangles in Fig. 8. The PLF triggers with $Z_{PLF} = 11$ and 20 were detected at 8.4° and 14.8°. The emission of neutrons from the TLF varies with the PLF kinetic energy in a manner similar to that of the LCP's.

Figure 9 shows the γ-ray fold distributions $P(k_\gamma)$ observed in coincidence with the PLF's having kinetic energies from the lowest- and highest-energy bins, respectively. Here we note that the k_γ distribution corresponding to the highest-energy bins shifts upward with PLF energy for the $Z_{PLF}=11$ case. The reverse is seen for the $Z_{PLF}=20$ fragments, where the highest-energy bin corresponds to quasielastic collisions. This can be interpreted as follows: the neutron multiplicity is a function of excitation energy of the system while γ-ray fold may be influenced significantly by the angular momentum. The $Z_{PLF} = 11$ produced with 100–200 MeV of kinetic energy may come on average from more central collisions than the $Z_{PLF} = 20$ case. In this case the

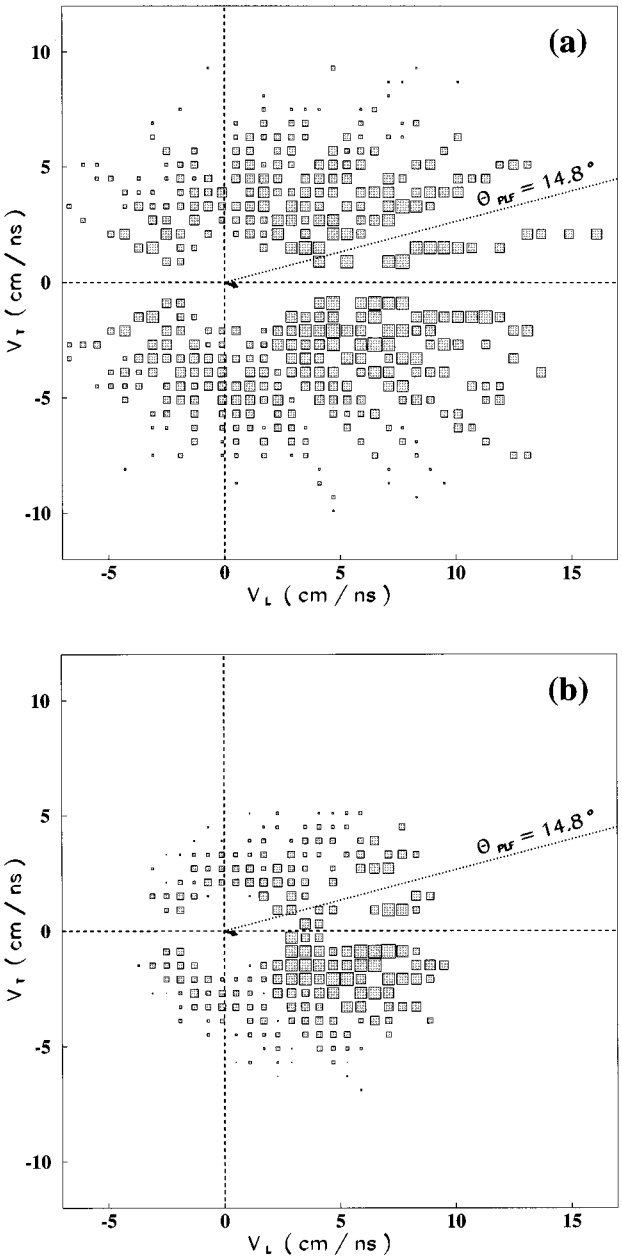

FIG. 4. Invariant cross section plots for (a) protons and (b) α-particle emitted in coincidence with $Z_{PLF} = 20$ fragments observed at 14.8° for the lowest-energy bin (300–400 MeV). The small arrows indicate the targetlike emitter velocity. The dotted line points to the projectilelike trigger detector. The box sizes are proportional to the logarithm of invariant cross section.

γ-cascade may be shorter due to lower spins in the system, despite the high excitation. In the $Z_{PLF} = 20$ case, the n and γ multiplicities trends agree because the primary system is likely to be created closer to the yrast line. The experimental k_γ fold distributions were converted into the TLF spin using the prescription given in Ref. [15].

IV. ANALYSIS

A. Event reconstruction procedure

The main goal of the event reconstruction procedure is to obtain primary fragment characteristics (mass, excitation en-

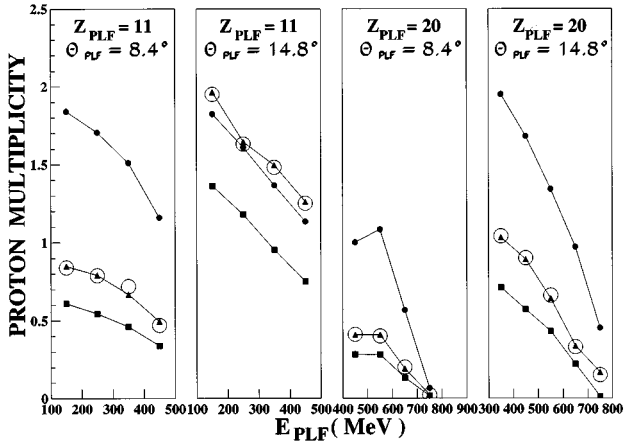

FIG. 5. Proton multiplicities. Those recorded by the DBW in coincidence with PLF's are shown by the closed circles. The raw multiplicities recorded at $\theta > 60°$ are shown as full squares and were used to deduce the proton multiplicities associated with the TLF's (triangles). The results of the statistical model calculations (see text) are given by the large open circles. The lines are drawn to guide the eye.

ergy, etc.). The term primary refers to the time after the preequilibrium phase of the reaction is terminated and the hot PLF's and TLF's are separated beyond the Coulomb barrier radius (see Sec. V). This goal was achieved by a two-step process. The first one consisted of the kinematical reconstruction of events. The second step of the procedure deals with the excitation energy division between the primary PLF and TLF. This step utilizes a deduced relationship between the excitation energy of the fragment and the multiplicities of the LCP's and neutrons, and the total γ-ray energy.

While the analysis was performed event-by-event, the unknown parameters for the events were substituted with the values of maximum likelihood for a selected class (PLF energy, atomic number, and detection angle) of events (see below).

1. The kinematical reconstruction

The kinematical reconstruction was performed assuming:

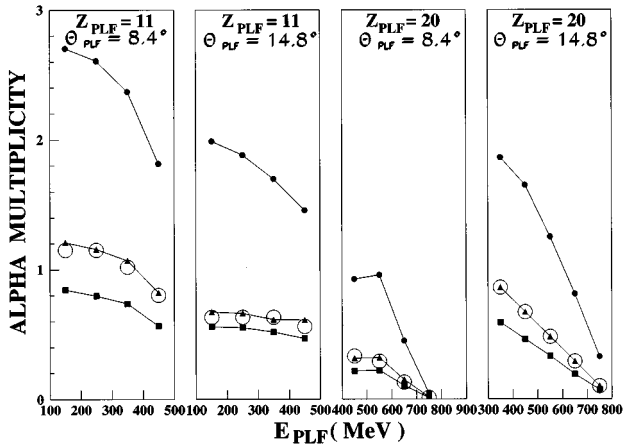

FIG. 6. Same as Fig. 5, but for α particles.

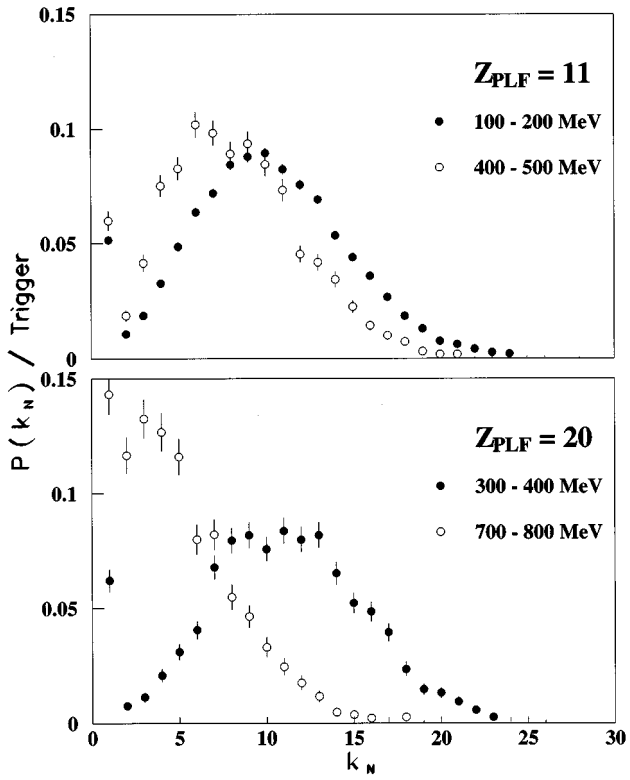

FIG. 7. Normalized neutron fold distributions measured in coincidence with the projectilelike triggers detected in the second ring of the DW detectors. The charge values Z_{PLF} and the bin energies are indicated.

(i) The preequilibrium emission of the beam velocity particle (BVP) precedes the binary splitting of the hot composite system.

(ii) The primary PLF and TLF each deexcite by a variety of decay modes, on a time scale such that the decays are only weakly influenced by the other primary fragment.

(iii) The velocity vectors of the primary PLF and TLF are preserved despite the emission during deexcitation.

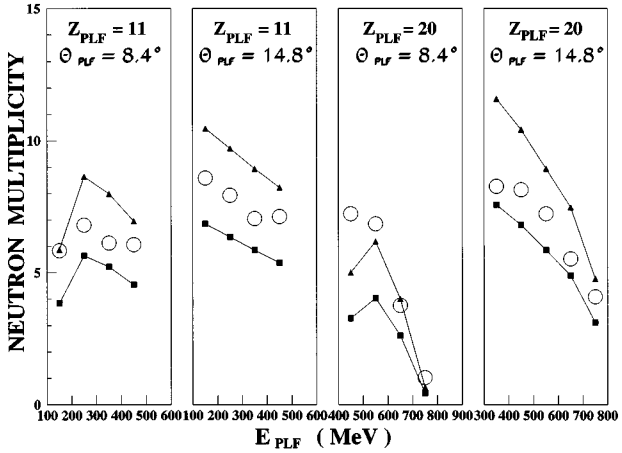

FIG. 8. Total neutron multiplicities (triangles) associated with emission from the TLF deduced from the neutrons recorded at the polar angle $\theta > 60°$ (squares) in coincidence with PLF triggers. The statistical model results (see text) are shown by the large open circles. The lines are drawn to guide the eye.

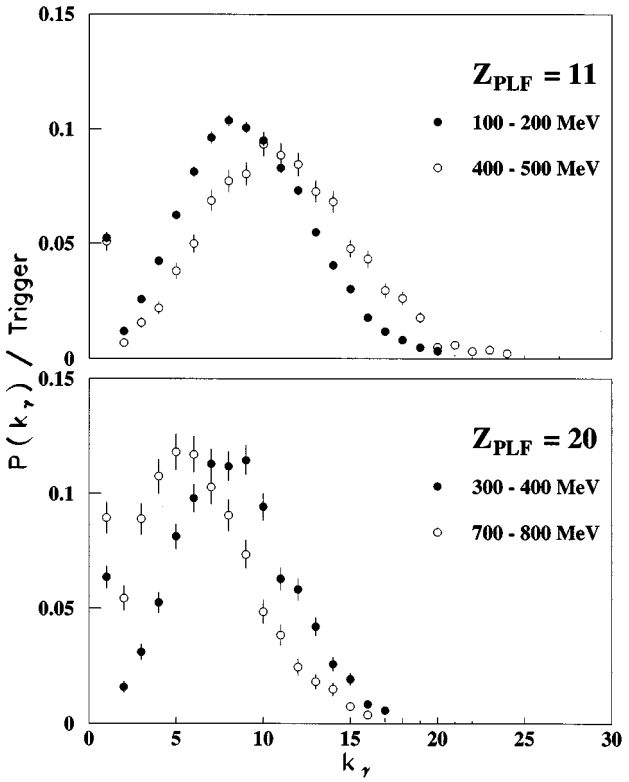

FIG. 9. γ-ray fold distributions $P(k_\gamma)$ observed in coincidence with the PLF's detected in the second ring of the DW detector. The fragment Z_{PLF} values and their associated bin energies are indicated.

Two equations of the linear momentum conservation at the end of the early phase of the reaction can be written

$$p_1 - p_{\overline{\mathrm{BVP}}} = p'_{\mathrm{PLF}}\cos\theta'_{\mathrm{PLF}} + p'_{\overline{\mathrm{TLF}}}\cos\theta'_{\overline{\mathrm{TLF}}} \tag{1}$$

and

$$0 = p'_{\mathrm{PLF}}\sin\theta'_{\mathrm{PLF}} + p'_{\overline{\mathrm{TLF}}}\sin\theta'_{\overline{\mathrm{TLF}}}, \tag{2}$$

where p_1 and $p_{\overline{\mathrm{BVP}}}$ are the linear momenta of the projectile and the BVP, respectively. The bar sign above the subscript is used to denote the variables associated with the fragments and particles which have not been observed experimentally. Solving of the above equations with respect to the linear momentum of the primary PLF one obtains

$$p'_{\mathrm{PLF}} = \frac{p_1 - p_{\overline{\mathrm{BVP}}}}{\cos\theta'_{\mathrm{PLF}} - \sin\theta'_{\mathrm{PLF}}\cot\theta'_{\overline{\mathrm{TLF}}}}. \tag{3}$$

From this we obtain the mass of the primary PLF as

$$m'_{\mathrm{PLF}} = \frac{1}{v'_{\mathrm{PLF}}}\,\frac{p_1 - m_{\overline{\mathrm{BVP}}}v_1}{\cos\theta'_{\mathrm{PLF}} - \sin\theta'_{\mathrm{PLF}}\cot\theta'_{\overline{\mathrm{TLF}}}}, \tag{4}$$

where $v'_{\mathrm{PLF}} = v_{\mathrm{PLF}}$ is the PLF velocity, measured experimentally, and v_1 is the beam velocity. In order to utilize Eq. (4) for the primary PLF mass determination, the mass of the BVP, $m_{\overline{\mathrm{BVP}}}$, and the emission angle of the TLF, $\theta'_{\overline{\mathrm{TLF}}}$, must be reconstructed. The latter quantity can be expressed as follows:

$$\theta'_{\overline{\mathrm{TLF}}} = \arcsin\frac{v^{\perp}_{\overline{\mathrm{TLF}}}}{|\vec{v}_{\overline{\mathrm{TLF}}}|}, \tag{5}$$

where $v^{\perp}_{\overline{\mathrm{TLF}}}$ and $|\vec{v}_{\overline{\mathrm{TLF}}}|$ are the transverse and total velocities of the TLF, respectively.

As shown in Sec. III (see Fig. 4), the reaction system is sufficiently asymmetric to allow us to use the difference in kinematic focusing of the emitted particles to distinguish the emission from the slowly moving TLF. In view of this, it was possible to obtain the value of TLF velocity.

To find the transverse velocity of the TLF, $v^{\perp}_{\overline{\mathrm{TLF}}}$, a transverse momentum analysis was applied to the experimental data. The equation of linear momentum conservation for the perpendicular component of the cold reaction products can be written as

$$0 = p^{\perp}_{\mathrm{PLF}} + p^{\perp}_{\overline{\mathrm{TLF}}} + p^{\perp}_{\mathrm{LCP}} + p^{\perp}_{\overline{\mathrm{LCP}}} + p^{\perp}_{N} + p^{\perp}_{\overline{N}}. \tag{6}$$

Again, we assumed that the transverse momentum of the BVP is equal to zero. This equation contains three elements which are not available from the experimental data, namely, the transverse momenta of the undetected TLF and LCP's, and the total transverse momentum of the neutrons (the SS detection system recorded only the neutron multiplicities angular distributions). A small fraction of the LCP's and neutrons escaped detection due to the limited acceptance of both detection systems. Therefore the missing transverse momentum $p^{\perp}_{\mathrm{MM}}$ can be defined

$$p^{\perp}_{\mathrm{MM}} = p^{\perp}_{\overline{\mathrm{TLF}}} + p^{\perp}_{\overline{\mathrm{LCP}}} + p^{\perp}_{N} + p^{\perp}_{\overline{N}}. \tag{7}$$

The missing transverse momentum is dominated by the transverse momentum of the undetected TLF. In order to calculate the last three terms of Eq. (7), we assumed that the neutrons and the undetected LCP's are emitted from one effective source, consisting of the contributions from the primary projectilelike and targetlike emitters. The perpendicular component of the source velocity for this effective source was calculated as follows:

$$v^{\perp}_{\mathrm{eff}} = \frac{m^{\mathrm{eff}}_{\mathrm{PLF}}}{m^{\mathrm{eff}}_{\mathrm{PLF}} + m^{\mathrm{eff}}_{\mathrm{TLF}}}v^{\perp}_{\mathrm{PLF}} + \frac{m^{\mathrm{eff}}_{\mathrm{TLF}}}{m^{\mathrm{eff}}_{\mathrm{PLF}} + m^{\mathrm{eff}}_{\mathrm{TLF}}}v^{\perp}_{\overline{\mathrm{TLF}}}, \tag{8}$$

where $m^{\mathrm{eff}}_{\mathrm{PLF}} = (m'_{\mathrm{PLF}} + m_{\mathrm{PLF}})/2$ and $m^{\mathrm{eff}}_{\mathrm{TLF}} = (m'_{\overline{\mathrm{TLF}}} + m_{\overline{\mathrm{TLF}}})/2$.

On the other hand, the missing transverse momentum is equal to

$$p^{\perp}_{\mathrm{MM}} = -p^{\perp}_{\mathrm{PLF}} - p^{\perp}_{\mathrm{LCP}}. \tag{9}$$

The momenta on the right side of Eq. (9) were measured in this experiment. Now, the transverse velocity of the TLF can be written as

$$v^{\perp}_{\overline{\mathrm{TLF}}} = \frac{-p^{\perp}_{\mathrm{PLF}} - p^{\perp}_{\mathrm{LCP}} - v^{\perp}_{\mathrm{eff}}(m_{\overline{\mathrm{LCP}}} + m_N + m_{\overline{N}})}{m_{\overline{\mathrm{TLF}}}}. \tag{10}$$

The undetected TLF mass is given by the equation of the mass conservation

$$m_{\overline{\mathrm{TLF}}}=m_P+m_T-m_{\mathrm{PLF}}-m_{\mathrm{LCP}}-m_{\overline{\mathrm{LCP}}}-m_N-m_{\overline{N}}-m_{\overline{\mathrm{BVP}}}. \tag{11}$$

The masses of the undetected LCP's, $m_{\overline{\mathrm{LCP}}}$, and the undetected neutrons can be calculated

$$m_{\overline{\mathrm{LCP}}}=m_{\mathrm{LCP}}\left(\frac{1}{f_{\mathrm{LCP}}}-1\right), \tag{12}$$

$$m_{\overline{N}}=m_N\left(\frac{1}{f_N}-1\right), \tag{13}$$

where $f_{\mathrm{LCP}}=0.93$ is the efficiency of the DBW to detect the LCP's and $f_N=0.87$ is the total triggering efficiency of the SS for neutrons.

The final step of our kinematical reconstruction procedure utilizes total energy conservation to determine the mass of the BVP's. The emission of the BVP's causes the available kinetic energy to decrease

$$T_P=T'_P-\frac{m_{\overline{\mathrm{BVP}}}v_P^2}{2}+Q_{\overline{\mathrm{BVP}}}, \tag{14}$$

where T'_P and $Q_{\overline{\mathrm{BVP}}}$ are the projectile kinetic energy and the Q value to emit the BVP particle, respectively, and v_P denotes the projectile velocity. Two scenarios for the emission of the BVP's were considered, namely, the BVP's escaped as one fragment or as a jet of free nucleons.

After the BVP's were emitted, a binary separation ensues, which produces the primary TLF and PLF. The effective projectile has mass, $m_P=m'_P-m_{\overline{\mathrm{BVP}}}$, and the available kinetic energy is shared as follows:

$$T_P+Q'=T'_{\mathrm{PLF}}+T'_{\mathrm{TLF}}, \tag{15}$$

where T'_{PLF} and T'_{TLF} are the kinetic energies of the primary PLF and TLF, respectively. The Q value Q' is determined by

$$Q'=Q_{gg}-E'^{*}_{\mathrm{PLF}}-E'^{*}_{\mathrm{TLF}}, \tag{16}$$

where Q_{gg} is a ground state Q value, E'^{*}_{PLF} and E'^{*}_{TLF} denote the excitation energies of the primary PLF and TLF, respectively. Supplementing Eq. (15) with the following two equations of momentum conservation

$$\sqrt{m_P T_P}=\sqrt{m'_{\mathrm{PLF}}T'_{\mathrm{PLF}}}\cos\theta'_{\mathrm{PLF}}+\sqrt{m'_{\mathrm{TLF}}T'_{\mathrm{TLF}}}\cos\theta'_{\mathrm{TLF}}, \tag{17}$$

$$0=\sqrt{m'_{\mathrm{PLF}}T'_{\mathrm{PLF}}}\sin\theta'_{\mathrm{PLF}}+\sqrt{m'_{\mathrm{TLF}}T'_{\mathrm{TLF}}}\sin\theta'_{\mathrm{TLF}}, \tag{18}$$

allows two independent prescriptions to be employed to calculate the Q value. One prescription can be used when the primary PLF energy T'_{PLF} and the emission angle θ'_{PLF} are measured:

$$Q'_{\mathrm{PLF}}=\frac{T_P(m_P-m'_{\mathrm{TLF}})+T'_{\mathrm{PLF}}(m'_{\mathrm{PLF}}+m'_{\mathrm{TLF}})-2\sqrt{m_P T_P m'_{\mathrm{PLF}}T'_{\mathrm{PLF}}}\cos\theta'_{\mathrm{PLF}}}{m'_{\mathrm{TLF}}}. \tag{19}$$

The second prescription can be used when the primary TLF energy T'_{TLF} and the emission angle θ'_{TLF} are measured or determined

$$Q'_{\mathrm{TLF}}=\frac{T_P(m_P-m'_{\mathrm{PLF}})+T'_{\mathrm{TLF}}(m'_{\mathrm{PLF}}+m'_{\mathrm{TLF}})-2\sqrt{m_P T_P m'_{\mathrm{TLF}}T'_{\mathrm{TLF}}}\cos\theta'_{\mathrm{TLF}}}{m'_{\mathrm{PLF}}}. \tag{20}$$

All quantities appearing in Eqs. (19) and (20) are given by Eqs. (4), (5), and (11), and depend on m_{BVP}. The obvious equation

$$Q'_{\mathrm{PLF}}=Q'_{\mathrm{TLF}} \tag{21}$$

makes the set of our equations complete, and all characteristics of the primary PLF and TLF can be reconstructed.

2. The numerical method and error estimations

The kinematical reconstruction procedure introduced in the preceding section is based on the conservation of energy, linear momentum, and mass. However, the resulting set of equations contains the experimental observables measured with statistical errors (e.g., the mass of the LCP's) and certain parameters which are known with limited accuracy (e.g., the laboratory angle, θ_{PLF}). In this situation, the standard solution of a set of the equations can (see, e.g., Ref. [17]), and does in the present case, become problematic (some results are pathological). This failure of the exact treatment comes from the fact that the problem is posed improperly. The equations and their solutions are strict and they contain mean values of observables in the literal, mathematical sense. The values measured experimentally are close to the statistical mean values. The correct (and reasonable) solutions may be found when, additionally, some method of statistical regularization of the solution is applied.

In our case besides the statistical uncertainty, the whole method is biased with the assumptions which are exactly true only for the exact mean values. We assumed that all parameters which are put in Eq. (21) may vary inside some definite interval. For instance, the laboratory angle of the PLF can be

any angle inside the range of the solid angle of the detector, and the mass of PLF can be any mass of the isotopes of the element Z_{PLF}, etc. Now, instead of solving Eq. (21), we performed the numerical procedure of minimization of the quantity

$$|Q'_{\mathrm{PLF}}-Q'_{\mathrm{TLF}}|^2. \tag{22}$$

The values of parameters needed to reach the minimum of Eq. (22) are considered to contain the statistically regularized solution of Eq. (21).

The uncertainty in the reconstruction procedure originates predominately from two sources. The first of them comes from the uncertainty of $Q_{\overline{\mathrm{BVP}}}$ which depends on the degree of clusterization of the BVP's. For the case of the emission as free mutually unbound nucleons, the most likely Q value was estimated to be

$$Q_{\overline{\mathrm{BVP}}}=-8\ \ [\mathrm{MeV}]m_{\overline{\mathrm{BVP}}}, \tag{23}$$

where 8 MeV stands for the average binding energy for a single nucleon. As any higher degree of clusterization of the BVP's yields a less negative Q value, it was assumed that the upper bound for the $Q_{\overline{\mathrm{BVP}}}$ is zero. The solutions of Eq. (22) for these two limiting values of $Q_{\overline{\mathrm{BVP}}}$ determine the limits of reasonable results and will be displayed as dashed areas in the subsequent figures.

At 19.1 MeV/nucleon preequilibrium emission can have a substantially lower energy and can even be deflected at angles covered by the DWB detection apparatus. The BVP velocity influences the reconstruction procedure through Eq. (14). It should be noted that the case of $Q_{\overline{\mathrm{BVP}}}=0$ is identical with the case of $Q_{\overline{\mathrm{BVP}}}=-8\ \ [\mathrm{MeV}]m_{\overline{\mathrm{BVP}}}$ and the energy of BVP of 11.1 MeV/nucleon, that is 58% of the beam energy. Therefore the reconstruction of data with $Q_{\overline{\mathrm{BVP}}}=0$ shows also what would be the trend of results if BVP velocity deviates from that of the beam.

The second significant source of error results from the ambiguity of solutions. It should be noted that $m_{\overline{\mathrm{BVP}}}$ in Eq. (23) is not known and, therefore, an iterative procedure was applied to manage this problem. Initially, the value of $Q_{\overline{\mathrm{BVP}}}$ is calculated for an arbitrary starting value $m^0_{\overline{\mathrm{BVP}}}$ and the reconstruction procedure is performed giving a new value of $m_{\overline{\mathrm{BVP}}}$. If $|m^0_{\overline{\mathrm{BVP}}}-m_{\overline{\mathrm{BVP}}}|>0$, then the reconstruction procedure is repeated. The calculations are repeated until $m^0_{\overline{\mathrm{BVP}}}$ and $m_{\overline{\mathrm{BVP}}}$ agree to within a preset value, which in this analysis was set to 2. This iteration procedure combined with the minimization of Eq. (22) leads to some dispersion of the reconstructed observables. In order to estimate the errors of the reconstructed observables, 10 independent procedures were performed; the maximum scatter of the derived observables is presented in the figures as vertical error bars.

The nondetection of the TLF makes it difficult to determine the primary TLF velocity. Its value and direction were found from the analyses of LCP's invariant cross sections and from the transversal momentum, respectively. This part of analysis causes some uncertainty, e.g., on the primary PLF mass, $\Delta m'_{\mathrm{PLF}}$, as a consequence of the uncertainty of the reconstruction of the TLF emission angle $\Delta\theta'_{\mathrm{TLF}}$. The typical error $\Delta\theta'_{\mathrm{TLF}}\simeq\pm\ 4.6°$ propagates on $\Delta m'_{\mathrm{PLF}}$ as the $\pm 2.8\%$ deviation. Therefore the primary PLF mass is confidently determined in 3 nucleon wide range.

3. The excitation energy division

The emission of the light particles (neutrons n, protons p, and alpha particles α) from the TLF (see Sec. III) was used to deduce its primary excitation energy. In order to derive the relationships between the multiplicities M_i (i=n, p, and α) of the light particles and the excitation energy, the statistical model code PACE [18] was used. Here we assumed emission from an excited nucleus with the mass obtained from the kinematical reconstruction and with the neutron to proton ratio close to the value of the target nucleus (see below). A spin value of the primary TLF was deduced [15] from the k_γ measurements. The application of the alternative method of the spin determination based on the angular distribution of $E2$ γ transitions [16] was not possible in this experiment. The excitation energy of the TLF source was adjusted to reproduce the experimental multiplicities for n, p, and α altogether. We required that the differences between the experimental and calculated multiplicities must be smaller than 5% and 20% for the LCP and neutron emissions, respectively. However, in order to achieve the agreement, small variations of the neutron to proton ratio and of the spin value were necessary. (Usually, the Z value of the primary TLF derived from the target's neutron to proton ratio was too large by up to three units.) This procedure yielded a remarkably good agreement between the calculated and experimental multiplicities (see Figs. 5, 6, and 8).

When the primary TLF excitation energy was established, Eq. (16) was used to obtain the primary PLF excitation energy.

B. Primary fragment characteristics

In this section we will present the primary fragment characteristics derived from the event reconstruction procedure. In Fig. 10 we display the deduced Q' value [see Eq. (16)] for the collisions when the $Z_{\mathrm{PLF}}=11$ and when $Z_{\mathrm{PLF}}=20$ fragments were detected at (a) 8.4° and (b) 14.8°, respectively. In this, and the following three figures, the dashed area displays the uncertainties of the reconstruction procedure (as mentioned above, this uncertainty is obtained by assuming either the emission of the BVP's as a single cluster or as a jet of separated nucleons). The vertical error bars represent the maximum scatter of the derived observables for 10 independent procedures of the reconstruction. The total mass of the BVP's (assumed to be emitted in the preequilibrium phase of the reaction) is shown in Fig. 11. The reconstructed PLF and TLF masses are shown in Figs. 12 and 13, respectively. Finally, the reconstructed primary PLF and TLF excitation energies per nucleon are given in Fig. 14.

Several noteworthy features of this analysis are apparent:

(1) Up to 30% of the projectile kinetic energy (917 MeV) is converted into internal excitation of the colliding nuclei (see Fig. 10).

(2) For the most violent collisions, a large fraction of the projectile kinetic energy (up to $\sim$ 400 MeV) is taken away in the early phase of the reaction by the BVP's (see Fig. 11).

(3) For the highest kinetic energy bin of the detected PLF, the primary TLF partner accepts almost all A_P-A_{PLF} nucle-

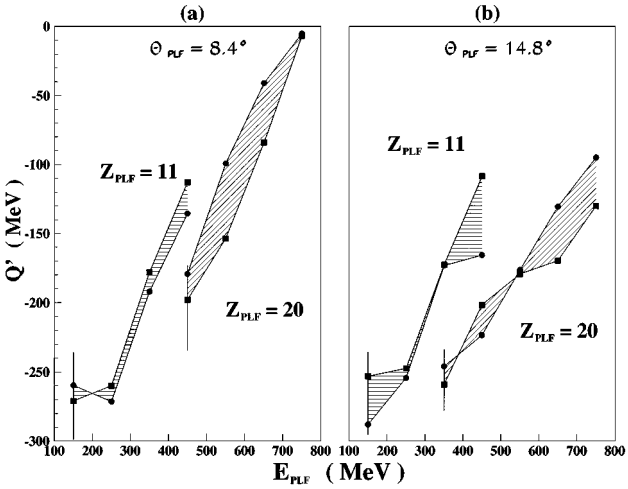

FIG. 10. Results of the kinematical reconstruction for the Q' value defined in Eq. (16). The Z_{PLF} = 11 and 20 fragments were detected at (a) 8.4° and (b) 14.8°. The borders of the dashed areas are the results of the reconstruction where the BVP's are emitted as (i) one cluster (circles) or (ii) a jet of separated nucleons (squares). The vertical error bars represent the maximum scatter of the derived observables for 10 independent procedures of the reconstruction. The mean results of this 10 reconstructions are drawn as squares.

ons and very few BVP's are emitted (see Figs. 12 and 13).

(4) If the kinetic energy of the detected PLF is reduced, thus driving up the amount of energy available for excitation (Q value becomes more negative), the primary PLF's become progressively heavier, while the primary TLF's become lighter than the target nuclei (see Figs. 12 and 13).

(5) For the lowest kinetic energy bins for the detected fragment $Z_{\mathrm{PLF}}=11$, the excitation energy is divided almost equally between the primary PLF and TLF partners (see Fig. 14). Taking into account the observation that in these deeply inelastic collisions the largest preequilibrium mass is emitted, these events can be visualized as a fast disintegration of the PLF nuclei.

(6) For the $Z_{\mathrm{PLF}}=20$ detected fragment, the excitation energy partition between the primary PLF and TLF approach the equal temperature limit (see Fig. 14).

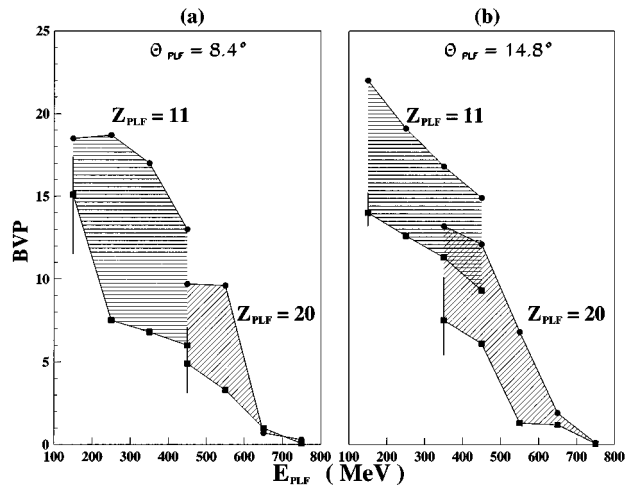

FIG. 11. Same as for Fig. 10 but for the BVP masses.

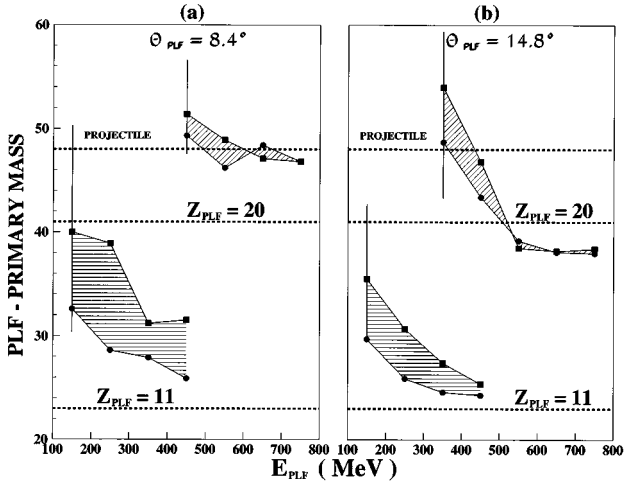

FIG. 12. Same as for Fig. 10 but for the primary PLF masses. The horizontal dotted lines indicate the projectile mass of ^{48}Ti and masses of the secondary PLF's. The PLF masses were estimated from detected Z_{PLF} values as $A_{\mathrm{PLF}}=2Z_{\mathrm{PLF}}+1$.

(7) For $Z_{\mathrm{PLF}}=20$ at 8.4 deg, the reconstructed primary PLF has a mass close to the projectile mass while the primary TLF has a lower mass than the target mass, the remaining mass being BVP. It looks like BVP has a TLF origin. This in turn implies that the true velocity of BVP may be smaller than the beam velocity, as discussed in Sec. IV A 2. The numerical method and error estimation.

V. MODEL CALCULATIONS

The primary PLF and TLF characteristics were calculated utilizing the molecular dynamics concept. The applied model [19], or rather its numerical implementation named CHIMERA (Code for Heavy Ion Medium Energy ReActions), is a combination of two recently devised models, namely, the Quantum Molecular Dynamics (QMD) model of Aichelin and Stöcker [20] and the Quasi-Particle Dynamics (QPD) model of Boal and Glosli [21]. The code is described in detail elsewhere [19,22] and here we shall specify its important characteristics:

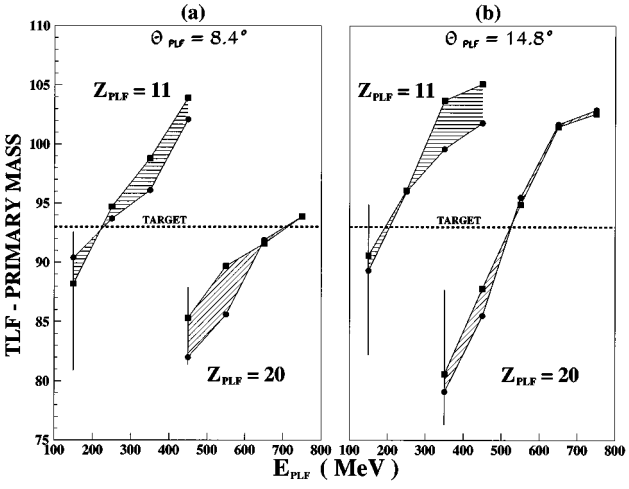

FIG. 13. Same as for Fig. 10 but for the primary TLF masses. The horizontal dotted line indicates the target mass of ^{93}Nb.

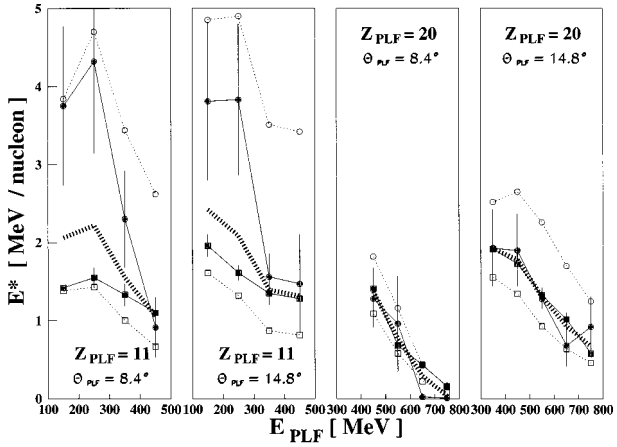

FIG. 14. Primary PLF (closed circles) and TLF (closed squares) excitation energies per nucleon obtained from the event reconstruction procedure. Open circles and squares indicate the hypothetical equal division of the excitation energy for PLF's and TLF's, respectively. Dashed lines give the hypothetical equal temperature division limits. Solid and dotted lines are drawn to guide the eye.

(1) The nucleons are represented by constant-width Gaussian wave packets obeying the minimal requirement of the uncertainty relation [20]. The centroid of the Gaussians are assumed to evolve along classical trajectories.

(2) The scattering of the nucleons is treated as if they were free (stochastic scattering with the experimental free nucleon-nucleon cross section). The collisions are statistically independent and the interference between two different collisions is neglected.

(3) The real part of the transition matrix is replaced by an effective potential. The nuclear effective potential was derived from a Skyrme parametrization of the potential energy density and was supplemented with the Coulomb potential and the momentum-dependent Pauli potential to simulate the fermionic nature of the nucleons. Calculations were performed for the nuclear potential corresponding to a soft equation of state (the nuclear matter compressibility $K \simeq 200$ MeV).

(4) The experimental values of the ground state binding energies and rms radii are well reproduced by the model calculations.

(5) The two colliding ions are assumed to move along classical Coulomb trajectories until the distance between their surfaces is 3 fm. The set of $6(A_P+A_T)$ equations of motion is solved numerically, where A_P and A_T are the projectile and target mass numbers, respectively.

A close inspection of the time evolution of the collision shows that the required time interval for the system to split into the PLF and TLF is dependent on the inelasticity of the collision (a stronger damping implies a later disintegration). This can be seen in Figs. 15(a) and 15(b) where the fragment mass and excitation energy distributions are plotted at the time when the binary splitting occurs. Here we note that as the separation time increases, both the mass and excitation energy distributions become broader.

Figure 16(a) displays a scatter plot (number of events) of the PLF versus TLF mass, as predicted by the model calculation. The calculated events were generated for collisions with impact parameters $0 \leqslant b \leqslant 9$ fm. The calculations were

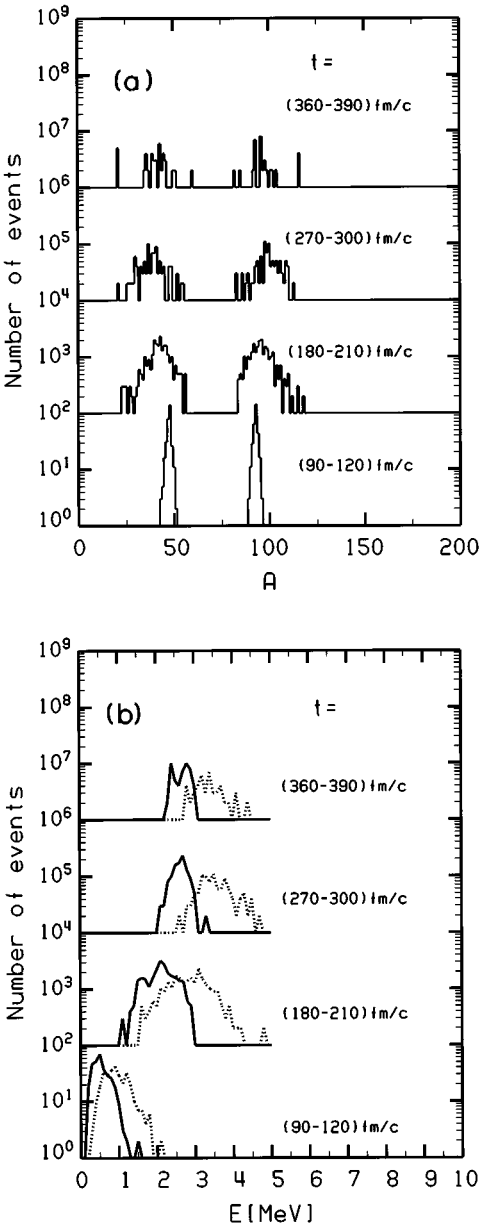

FIG. 15. (a) Fragment mass and (b) excitation energy/nucleon distributions obtained from QMD calculation. The excitation energy distributions are drawn as solid and broken lines for TLF's and PLF's, respectively. The distributions are plotted for fragments from binary split within indicated time intervals t.

terminated at 450 fm/c when the binary splitting into the PLF ($20 \leqslant A_{\mathrm{PLF}} \leqslant 60$) and TLF ($70 \leqslant A_{\mathrm{TLF}} \leqslant 120$) ceases. The reconstructed experimental data are shown in Fig. 16(b). There is an obvious difference between the model calculations and the reconstructed data, namely, that the total mass of the reconstructed PLF and TLF is considerably lower than from the simulation except for the least damped collisions leading to $Z_{\mathrm{PLF}}=20$ fragments. In Fig. 17 we show the scatter plot of the TLF versus PLF excitation energy. The calculated events were sorted with respect to the PLF and TLF masses, the PLF velocity, and detection angle. These conditions were selected to match the reconstructed events producing $Z_{\mathrm{PLF}}=20$ fragments detected in the second ring of the detectors with the kinetic energy of the fifth bin (see Fig. 3).

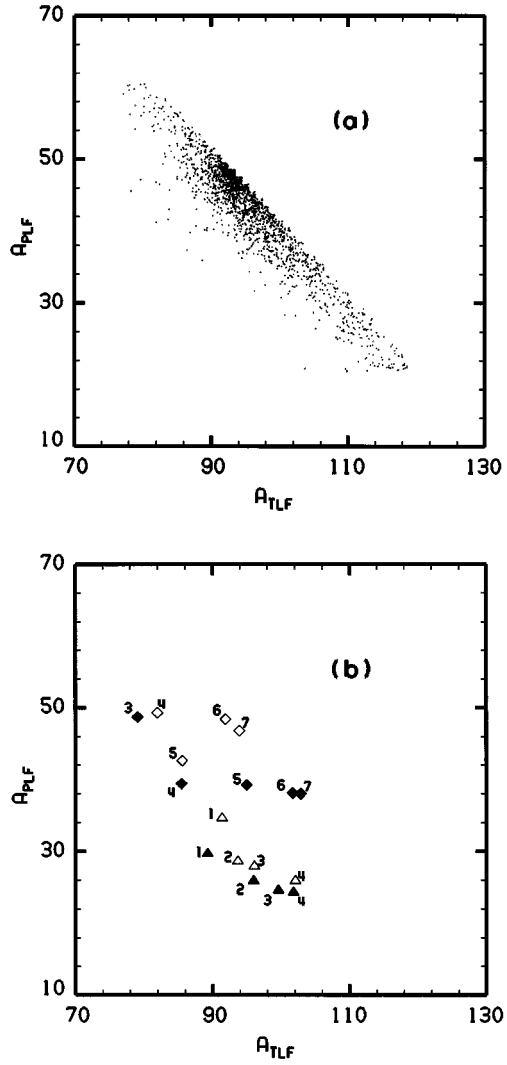

FIG. 16. (a) Scatter plot of the masses of the second heaviest vs the heaviest fragment from the QMD calculations (see text for the sorting conditions). (b) Primary PLF and TLF masses obtained from the reconstruction procedure for the $Z_{PLF}=11$ (diamonds) and $Z_{PLF}=20$ (triangles) for the PLF's detected at 8.4° (open symbols) and 14.8° (full symbols).

The experimental value obtained from the reconstruction procedure (and the statistical model calculations) is marked as the star. Here we note that both the experiment and the model calculations predict equal excitation energy per nucleon of the primary PLF and TLF. However, the predictions from the model calculation are higher than the experimental values by (10–20)%.

A quantitative discrepancy between the CHIMERA code results and the reconstructed experimental data may be a consquence of the nucleon—nucleon interaction used in our model. This study of, as well as the extensive model calculation, are in progress.

VI. SUMMARY

The primary fragment characteristics were studied in reactions of ^{48}Ti + ^{93}Nb at 19.1 MeV/nucleon. The excitation energy partition between the primary PLF and TLF was reconstructed by a procedure developed which utilized the information provided by two 4π detection systems. The experimental results were compared to one of the most advanced microscopic treatments of the dynamics of heavy ion collisions.

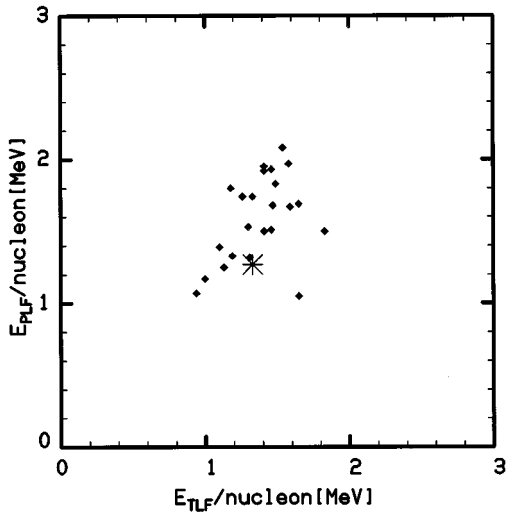

FIG. 17. Scatter plot of the TLF versus PLF excitation energies. The calculated events were sorted with respect to the PLF and TLF masses, the PLF velocity, and detection angle (see text). The result obtained from the reconstruction procedure and statistical model calculations is shown as the star.

The trends in the reconstructed primary fragment excitation energies and masses cannot be reconciled with any single process. We can however reconcile the observed trends seen in the data by considering a mixture of those features expected from strongly damped collisions and those expected for the projectile fragmentation [14].

First, we will consider those events producing the observed fragments with charge only slightly less than that of the projectile ($Z_{PLF}=20$). We observe that the excitation energy divisions are always weighted towards the target. For the smaller energy losses, the mass flow is also towards the target. With increasing energy loss the mass flow moves towards symmetry, but the available excitation energy remains divided in proportion to the primary PLF and TLF masses (equal temperature regime). This finding is at odds with the often cited concept that energy goes to where the mass flows [23]. However, excitation can be generated in both the primary PLF and TLF even when the net mass transferred is equal to zero as long as there has been a flow of nucleons in both directions. Moreover, it has been noted that the stripped nucleus may acquire excitation via a hole generation process [24].

Our other case, events producing final fragments with only half of the mass of the projectile, have excitation energy partitions which change from being biased toward the target (for smaller energy losses) to nearly equal partition (for the largest energy losses). Here we can understand the smaller energy losses as resulting from massive transfers which increases the mass of the target at the expense of the projectile, leaving the primary TLF with more excitation than the primary PLF. The counter intuitive evolution toward equal energy division with increasing damping is we suspect a trivial

result of our selection of low mass of the detected fragments. Specifically, the dominant mechanism for producing these final fragments with the mass far from the projectile is from the fragmentation of the projectile that has unusually large excitation energy.

An essential feature of the CHIMERA code calculations is that the model predicts a higher temperature of the PLF's and TLF's and a lower preequilibrium mass loss than is observed.

In summary, we conclude that, at 20 MeV/nucleon projectile energy, the interactions between heavy ions show phenomena, which at present can be only understood phenomenologically with a combination of models. While a quantum-molecular dynamics model has some success at reproducing selected features of the data, on the whole this model falls far short of a quantitative description of these data.

ACKNOWLEDGMENTS

One of us (Z.M.) would like to thank Prof. D. G. Sarantites for his kind hospitality during his stay at Washington University in St. Louis. This work was supported by the Director, Office of Energy Research, Office of High Energy and Nuclear Physics, Nuclear Physics Division of the U.S. Department of Energy, under Grant Nos. DE-FG02-88-ER40406 and DE-FG02-87-ER40316. Oak Ridge National Laboratory is managed by Martin Marietta Energy System, Inc. under Contract No. DE-AC05-84OR21400 with the Department of Energy.

[1] W. U. Schröder and J. R. Huizenga, in *Treatise on Heavy-Ion Science*, edited by D. A. Bromley (Plenum Press, New York, 1984), Vol. 2, p. 115, and references therein.

[2] D. Hilscher, in *Proceedings of the Specialist Meeting on Preequilibrium Nuclear Reactions*, Semmering, Austria, 1988, edited by B. Strohmeyer (Institut fur Radiumforschung und Kerphysik, Universität Vienna, 1988), p. 245.

[3] L. G. Moretto and G. J. Wozniak, Annu. Rev. Nucl. Part. Sci. **43**, 379 (1993), and references therein.

[4] R. J. Charity, J. Barreto, L. G. Sobotka, D. G. Sarantites, D. W. Stracener, A. Chbihi, N. G. Nicolis, R. Auble, C. Baktash, J. R. Beene, F. Bertrand, M. Halbert, D. C. Hensley, D. J. Horen, C. Ludemann, M. Thoennessen, and R. Varner, Phys. Rev. C **46**, 1951 (1992).

[5] B. Lott, S. P. Baldwin, B. M. Szabo, B. M. Quednau, W. U. Schröder, J. T̃oke, L. G. Sobotka, J. Barreto, R. J. Charity, L. Gallamore, D. G. Sarantites, D. W. Stracener, and R. T. de Souza, Phys. Rev. Lett. **68**, 3143 (1992).

[6] L. G. Sobotka, Z. Majka, D. W. Stracener, D. G. Sarantites, R. J. Charity, G. Auger, E. Plagnol, Y. Schutz, R. Dayras, J. P. Wieleczko, J. Barreto, and E. Norbeck, in *Nuclear Physics at GANIL 1992-1993*, edited by M. Bex and J. Galin (Ganil, Caen, France, 1993), p. 150

[7] J. Péter, S. C. Jeong, J. C. Angélique, G. Auger, G. Bizard, R. Brou, A. Buta, C. Cabot, Y. Cassagnou, E. Crema, D. Cussol, D. Durand, Y. El Masri, P. Eudes, Z. Y. He, A. Karembrun, C. Lebrun, R. Legrain, J. P. Patry, A. Péghaire, R. Régimbart, E. Rosato, F. Saint-Laurent, J. C. Steckmeyer, B. Tamain, and E. Vient, Nucl. Phys. **A593**, 95 (1995).

[8] B. M. Quednau, S. P. Baldwin, B. Lott, W. U. Schröder, B. M. Szabo, J. T̃oke, D. Hilscher, U. Jahnke, H. Rossner, S. Bresson, J. Galin, D. Guerreau, M. Morjean, and D. Jacquet, Phys. Lett. B **309**, 10 (1993); J. F. Lecolley, L. Stuttgé, M. Aboufirassi, A. Badala, B. Bilwes, R. Bougault, R. Brou, F. Cosmo, J. Colin, D. Durand, J. Galin, A. Genoux-Lubain, D. Guerreau, D. Horn, D. Jacquet, J. L. Laville, F. Lefebvres, C. Le Brun, J. Lemiére, O. Lopez, M. Louvel, M. Mahi, M. Morjean, C. Paulot, A. Péghaire, N. Prot, G. Rudolf, F. Scheibling, J. C. Steckmeyer, B. Tamain, and S. Tomasevic, Phys. Lett. B **325**, 317 (1994).

[9] J. Randrup, Nucl. Phys. **A447**, 133c (1985).

[10] Z. Majka, V. Abenante, Z. Li, N. G. Nicolis, D. G. Sarantites T. M. Semkow, L. G. Sobotka, D. W. Stracener, J. R. Beene, D. C. Hensley, and H. C. Griffin, Phys. Rev. C **40**, 2124 (1989).

[11] R. Płaneta, K. Kwiatkowski, S. H. Zhou, V. E. Viola, H. Breuer, M. A. McMahan, J. Randrup, and A. C. Mignerey, Phys. Rev. C **39**, 1197 (1989).

[12] D. W. Stracener, D. G. Sarantites, L. G. Sobotka, J. Elson, J. T. Hood, Z. Majka, V. Abenante, A. Chbihi, and D. C. Hensley, Nucl. Instrum. Methods Phys. Res. A **294**, 485 (1990).

[13] M. Jääskeläinen, D. G. Sarantites, R. Woodward, F. A. Dilmanian, J. T. Hood, R. Jääskeläinen, D. C. Hensley, M. Halbert, and J. H. Barker, Nucl. Instrum. Methods Phys. Res. **204**, 385 (1983).

[14] P. Staszel, Z. Majka, L. G. Sobotka, V. Abenante, N. G. Nicolis, D. G. Sarantites, D. W. Stracener, C. Baktash, M. L. Halbert, and D. C. Hensley, Phys. Lett. B **368**, 26 (1996).

[15] D. G. Sarantites, L. Westerberg, M. L. Halbert, R. A. Dayras, D. C. Hensley, and J. H. Barker, Phys. Rev. C **18**, 774 (1978).

[16] L. G. Moretto, Nucl. Phys. **A387**, 331c (1982).

[17] M. Dakowski, Yu. A. Lazarev, V. F. Turchin, and L. S. Turovtseva, Nucl. Instrum. Methods **113**, 113 (1973).

[18] A. Gavron, Phys. Rev. C **21**, 230 (1980).

[19] J. Łukasik and Z. Majka, Acta Phys. Pol. B **24**, 1959 (1993).

[20] J. Aichelin and H. Stöcker, Phys. Lett. B **176**, 14 (1986); J. Aichelin, Phys. Rep. **202**, 233 (1991).

[21] D. H. Boal and J. N. Glosli, Phys. Rev. C **38**, 1870 (1988); D. H. Boal and J. N. Glosli, Phys. Rev. C **38**, 2621 (1988).

[22] J. Łukasik, Z. Majka, and T. Kozik, Phys. Lett. B **318**, 419 (1993).

[23] B. Cauvin, R. C. Jared, P. Russo, R. P. Schmitt, R. Babinet, and L. G. Moretto, Nucl. Phys. **A301**, 511 (1978).

[24] Z. Sosin, K. Grotowski, A. Wieloch, and H. W. Wilschut, Acta Phys. Pol. B **25**, 1601 (1994).